4204 *Chem. Mater.* **2010,** *22,* 4204–4213
DOI:10.1021/cm1011586

CHEMISTRY OF MATERIALS
Article

Layered Rare-Earth Hydroxides (LRHs) of $(Y_{1-x}Eu_x)_2(OH)_5NO_3 \cdot nH_2O$ ($x = 0-1$): Structural Variations by Eu^{3+} Doping, Phase Conversion to Oxides, and the Correlation of Photoluminescence Behaviors

Qi Zhu,[†,‡] Ji-Guang Li,*[,†,‡] Chunyi Zhi,[§] Xiaodong Li,[†] Xudong Sun,[†] Yoshio Sakka,[∥,¶] Dmitri Golberg,[§] and Yoshio Bando[§]

[†]*Key Laboratory for Anisotropy and Texture of Materials* (*Ministry of Education*), *School of Materials and Metallurgy, Northeastern University, Shenyang, Liaoning 110004, China,* [‡]*Nano Ceramics Center, National Institute for Materials Science, Namiki 1-1, Tsukuba, Ibaraki 305-0044, Japan,* [§]*World Premier International Center for Materials Nanoarchitectonics* (*MANA*), *National Institute for Materials Science, Namiki 1-1, Tsukuba, Ibaraki 305-0044, Japan,* [∥]*Nano Ceramics Center, National Institute for Materials Science, Sengen 1-2-1, Tsukuba, Ibaraki 305-0047, Japan, and* [¶]*World Premier International Center for Materials Nanoarchitectonics* (*MANA*), *National Institute for Materials Science, Sengen 1-2-1, Tsukuba, Ibaraki 305-0047, Japan*

Received April 26, 2010. Revised Manuscript Received June 18, 2010

Layered hydroxides of $(Y_{1-x}Eu_x)_2(OH)_5NO_3 \cdot nH_2O$ ($x = 0-1$) have been hydrothermally synthesized under the optimized conditions of 120 °C and pH ~7.0. Eu incorporation yields steadily smaller particles, elongation of the well-developed hexagon platelets, and linearly expanded *ab* planes of the layered structure. The interlayer distance ($c/2$), closely related to the hydration number n, is inversely proportional to the Eu content. The systematically changing photoluminescence behaviors allow to conclude that a lower hydration shifts the Eu^{3+} coordination from C_{4v} to C_1 symmetries and that the C_1-site Eu^{3+} is significantly associated with the 595 nm $^5D_0 \rightarrow {}^7F_1$ and the 615 nm $^5D_0 \rightarrow {}^7F_2$ transitions while the C_{4v}-site Eu^{3+} with the 589 nm $^5D_0 \rightarrow {}^7F_1$ and the 698 nm $^5D_0 \rightarrow {}^7F_4$ transitions. The hydroxides convert to cubic $(Y_{1-x}Eu_x)_2O_3$ at temperatures ≥400 °C while retaining the original morphologies. The best luminescence was observed for the oxides at $x = 0.05$ for the 613-nm red emission, and significant quenching of luminescence occurred at $x > 0.10$. Red shift of the charge-transfer excitation band was observed to be due to the elongated Eu−O bond arising from lattice expansion. The asymmetry factor of luminescence, $I(^5D_0 \rightarrow {}^7F_2)/I(^5D_0 \rightarrow {}^7F_1)$, exhibits a sharp increase from ~11.4 at $x = 0.5$ to ~23 at $x = 1.0$, which has been ascribed to the splitting of C_1 symmetry from distorted S_6 sites.

Introduction

Layered rare-earth hydroxides (LRHs), possessing a general formula of $Ln_8(OH)_{20}(A^{m-})_{4/m} \cdot nH_2O$ (Ln = rare-earth ions; A = intercalated anions), were first prepared by Gándara et al. via hydrothermal treatment of rare-earth nitrates in the presence of triethylamine (Et_3N).[1] The LRHs and the common layered double hydroxides (LDHs, $[M^{2+}_{1-x}M^{3+}_x(OH)_2]^{x+}[A^{m-}_{x/m}]^{x-} \cdot nH_2O$) both belong to the anion type of inorganic layered compounds, but the LRHs have only one type of cations (Ln^{3+}) in the host layer. Because of the unique electronic, optical, magnetic, and catalytic properties of the rare-earth elements, LRHs have attracted immediate attention since their emergence, and extensive efforts have been paid to their synthesis, structural characterization, anion exchanges, and exfoliation. Fogg et al.[2a−d] first synthesized the novel family of anion-exchangeable $Ln_2(OH)_5NO_3 \cdot xH_2O$ (Ln = Y, Gd−Lu; $x = 1-1.5$) via autoclaving the corresponding $Ln(NO_3)_3 \cdot xH_2O$ solution in the presence of NaOH and $NaNO_3$. They found that it is difficult for larger lanthanides to form LRHs and suspected that Gd might be the boundary. They also found that the degree of hydration would affect structural features of the layered phases. The nitrate ions were shown to exist in the interlayer gallery, not coordinated to Ln^{3+}, thus exhibiting facile exchanges with a wide range of organic carboxylate and sulfonate anions. Furthermore, the interlayer distance is significantly affected by the size of the intercalated anions and can be expanded from ~0.9 nm for the pristine LRHs to ~2.4 nm for the intercalated ones, revealing that the LRHs may potentially be exfoliated into single nanosheets for the further construction of various nanostructures, particularly

*Author to whom correspondence should be addressed. Tel.: +81-29-860-4394. Fax: +81-29-860-4701. E-mail: LI.Jiguang@nims.go.jp.

(1) Gándara, F.; Perles, J.; Snejko, N.; Iglesias, M.; Gómez-Lor, B.; Gutiérrez-Puebla, E.; Monge, M. A. *Angew. Chem., Int. Ed.* **2006**, *45*, 7998.
(2) (a) McIntyre, L. J.; Jackson, L. K.; Fogg, A. M. *J. Phys. Chem. Solids* **2008**, *69*, 1070. (b) McIntyre, L. J.; Jackson, L. K.; Fogg, A. M. *Chem. Mater.* **2008**, *20*, 335. (c) Hindocha, S. A.; McIntyre, L. J.; Fogg, A. M. *J. Solid State Chem.* **2009**, *182*, 1070. (d) McIntyre, L. J.; Prior, T. J.; Fogg, A. M. *Chem. Mater.* **2010**, *22*, 2635. (e) Poudret, L.; Prior, T. J.; McIntyre, L. J.; Fogg, A. M. *Chem. Mater.* **2008**, *20*, 7447.

 Published on Web 07/02/2010

highly transparent functional films. Fogg et al.[2e] have also succeeded in preparing the halide counterpart $[Ln_2(OH)_5X\cdot 1.5H_2O$, (X = Cl^-, Br^-; Ln = Y, Dy, Er, Yb)] of the nitrate family by replacing the nitrate with halide starting materials, and nicely revealed that the Cl^- and Br^- ions in the interlayer could also undergo facile exchanges at room temperature with a range of organic dicarboxylate anions. Through proper pH control of the hydrothermal reaction, Byeon et al.[3a] extended the nitrate family of LRHs to bigger elements of Gd, Eu, and Sm, and single phases were obtained in the three cases. The ion-exchange reactions of NO_3^- with diverse organic anions were successfully carried out in the interlayer gallery of LRHs, and the pristine layered gadolinium hydroxide and its long alkyl chain anion-exchanged derivative were shown to have a similar paramagnetic behavior. Byeon et al.[3b] further extended the nitrate family to even larger elements of Nd and La, by adopting a nonaqueous solvothermal reaction with ethanol containing alkali-metal hydroxide as the solvothermal medium. Though some alkali-metal nitrate remains in the interlayer gallery of the products, the layered compounds were shown to undergo exchange with some organic anions such as decanoate, decanesulfonate, and decylsulfate. More recently, a series of LRHs, $[Ln_8(OH)_{20}(H_2O)_n][A^{m-}]_{4/m}$ (Ln = Nd, Sm, Eu, Gd, Tb, Dy, Ho, Er, Tm, Y; A^{m-} = NO_3^- or Cl^-, $n \approx$ 6−8), with single-phase products for Sm−Er and Y have been synthesized by Sasaki et al.[4] via homogeneous precipitation through refluxing aqueous solutions containing the corresponding Ln salt and hexamethylenetetramine, and the correlation of particle morphology, lattice parameters, interlayer distance, hydration capability and crystal structure with the atomic number of Ln were systematically described. Through Rietveld refinement of the high-resolution XRD patterns obtained with synchrotron irradiation facilities, they were able to show that two types of Ln environments exist in $Ln_2(OH)_5A\cdot nH_2O$ (A = NO_3^- and Cl^-), that is, 8-fold coordinated $[Ln(OH)_7H_2O]$ and 9-fold coordinated $[Ln(OH)_8H_2O]$.[4a] Each LnO_8 polyhedron is linked to two other LnO_8 polyhedra and four LnO_9 polyhedra via edge sharing, and the linked polyhedron units then form a two-dimensional host layer parallel to the *ab* plane. The A^- anion species are mainly in the interlayer supporting the layers, and the loss of coordinated water molecules will result in an abrupt layer contraction. They found that the hydration number tends to decrease with increasing atomic number for the chloride family but increases for the nitrate analogue.[4] Morphology of the LRHs platelets was demonstrated to vary systematically with the atomic number of Ln.[4c] Characteristic emissions of the Eu^{3+} and Tb^{3+} ions were observed from the layered hydroxides of $Eu_8(OH)_{20}(NO_3)_4\cdot 7H_2O$ and $Tb_8(OH)_{20}Cl_4\cdot 7.0H_2O$, respectively, despite the presence of a large number of hydroxyls and water molecules.[4] Exfoliation of DS^- (dodecyl sulfate) decorated $Eu(OH)_{2.5}Cl_{0.5}\cdot 0.9H_2O$ and $Gd_2(OH)_5(NO_3)\cdot nH_2O$ in formamide to produce positively charged nanosheets have been achieved by Hu et al.[5] and Byeon et al.[6]

It was noticed that the previous studies largely focused on the synthesis, structure characterization, and anion exchanges of single lanthanide LRHs, while reports on LRH solid solutions have been rather limited. The formation of LRH solid-solutions would definitely widen the practical applications of the materials, as it allows functionality optimization through facile combination of different Ln and through adjusting the relative contents of the Ln elements. Hu et al.[5] constructed transparent films with $(Gd,Eu)_2(OH)_5Cl\cdot 1.8H_2O$ cubic particles and reported that the annealing-resultant highly [111] oriented Gd_2O_3:Eu films exhibit significantly stronger emission than the originally [001] oriented LRH films and also better than the powder form. Positively charged L(Gd, Eu)H nanosheets were obtained by Byeon el al.[6] via exfoliation of the LRHs solid solution in formamide and applied to fabricate highly transparent Gd_2O_3:Eu luminescent films by subsequent annealing. A systematic study, however, still lacks on the doping effects on structural features of the LRHs compounds, structure evolution upon conversion to oxides, and particularly the related luminescence phenomena as well as the origins of luminescence. In the present work, we synthesized a whole series of $(Y_{1-x}Eu_x)_2(OH)_5NO_3\cdot nH_2O$ (x = 0−1) LRHs via hydrothermal treatment of mixed nitrate solutions containing ammonium hydroxide and sometimes ammonium nitrate as a mineralizer. The above-mentioned issues were then investigated via detailed characterizations of the materials by combined techniques of XRD, TG, FT-IR, FE-SEM, HR-TEM, and PLE/PL spectroscopy. PL spectroscopy was demonstrated to be an efficient tool to probe the delicate structure (coordination environment) changes induced by doping and by thermal decomposition of the LRHs. The Y/Eu solid-solution form of LRH was chosen here as a model system because it is one of the most important red phosphors finding wide applications in areas such as fluorescent lamps, white light emitting diodes (white LEDs), plasma display panels (PDPs), flat panel displays (FDPs), field emission displays (FEDs), and cathode ray tubes (CRTs).[7] We believe that the outcomes of this work may enrich the applications of the LRH materials and may have wide implications to other LRH solid solution systems.

(3) (a) Lee, K.-H.; Byeon, S.-H. *Eur. J. Inorg. Chem.* **2009**, 929. (b) Lee, K.-H.; Byeon, S.-H. *Eur. J. Inorg. Chem.* **2009**, 4727.

(4) (a) Geng, F. X.; Matsushita, Y.; Ma, R.; Xin, H.; Tanaka, M.; Izumi, F.; Iyi, N.; Sasaki, T. *J. Am. Chem. Soc.* **2008**, *130*, 16344. (b) Geng, F. X.; Xin, H.; Matsushita, Y.; Ma, R.; Tanaka, M.; Izumi, F.; Iyi, N.; Sasaki, T. *Chem.—Eur. J.* **2008**, *14*, 9255. (c) Geng, F. X.; Matsushita, Y.; Ma, R.; Xin, H.; Tanaka, M.; Iyi, N.; Sasaki, T. *Inorg. Chem.* **2009**, *48*, 6724.

(5) (a) Hu, L. F.; Ma, R.; Ozawa, T. C.; Sasaki, T. *Angew. Chem., Int. Ed.* **2009**, *48*, 3846. (b) Hu, L. F.; Ma, R.; Ozawa, T. C.; Geng, F. X.; Iyi, N.; Sasaki, T. *Chem. Commun.* **2008**, 4897. (c) Hu, L. F.; Ma, R.; Ozawa, T. C.; Sasaki, T. *Chem. Asian J.* **2010**, *5*, 248. (d) Hu, L. F.; Ma, R.; Ozawa, T. C.; Sasaki, T. *Inorg. Chem.* **2010**, *49*, 2960.

(6) Lee, K.-H.; Lee, B. I.; You, J. H.; Byeon, S.-H. *Chem. Commun.* **2010**, *46*, 1461.

(7) (a) Blasse, G.; Grabmair, B. C. *Luminescent Materials*; Springer−Verlag: Berlin, 1994. (b) Buijs, M.; Meyerink, A.; Blasse, G. *J. Lumin.* **1987**, *37*, 9. (c) Pappalardo, R. G.; Hunt, R. B., Jr. *J. Electrochem. Soc.* **1985**, *132*, 721. (d) Forest, H.; Ban, G. *J. Electrochem. Soc.* **1969**, *116*, 474.

Experimental Section

Synthesis. The yttrium and europium sources for LRH solid solution synthesis are $Y(NO_3)_3 \cdot 6H_2O$ (99.99% pure, Kanto Chemical Co., Inc., Tokyo, Japan) and $Eu(NO_3)_3 \cdot 6H_2O$ (99.95% pure, Kanto Chemical Co., Inc.), respectively. In a typical synthetic procedure, a proper amount of ammonium hydroxide solution (25%, Wako Chemical Co., Inc., Tokyo) was added to 70 mL of a 2 mmol $M(NO_3)_3$ (M = Y and Eu) mixed solution for pH control. The resultant suspension was then transferred into a Teflon lined stainless-steel autoclave of 100 mL capacity after being constantly stirred for 30 min. The autoclave was tightly sealed and was put in an electric oven preheated to various temperatures in the range 120−200 °C to investigate the effects of reaction temperature on phase structure of the product. After 24 h of reaction, the autoclave was left to cool naturally to room temperature, and the hydrothermal product was collected via centrifugation. The wet precipitate was washed with distilled water for three times to remove the byproducts, rinsed with absolute ethanol, and was finally dried in air at 60 °C for 24 h to yield a white powder for further characterizations. $(Y_{1-x}Eu_x)_2O_3$ (x = 0−1) solid solutions was obtained by calcining the LRH precursors under flowing O_2 gas (200 mL/min) at selected temperatures for 4 h with a heating rate of 2 °C/min at the ramp stage.

Characterization Techniques. Phase identification was performed by X-ray diffractometry (XRD, Model RINF 2200 V/PC, Rigaku, Tokyo) operating at 40 kV/40 mA using nickel-filtered Cu Kα radiation and a scanning speed of 1.0° 2θ/min. Fourier transform infrared spectroscopy (FT-IR) (Model 7000e, Varian, Palo Alto, CA) of the precursors was performed by the standard KBr method. Morphologies of the products were observed via field-emission scanning electron microscopy (FE-SEM, Model S-5000, Hitachi, Tokyo) under an acceleration voltage of 10 kV and transmission electron microscopy (TEM, Model FEM-3000F, JEOL, Tokyo) operated at 300 kV. Thermogravimetry (TG, Model Thermo Plus TG8120, Rigaku, Tokyo) of the dried precursor was made in stagnant air with a heating rate of 10 °C/min. Photoluminescence (PL) and photoluminescence excitation (PLE) spectra of the LRHs and their calcination products were measured at room temperature using an FP-6500 fluorescence spectrophotometer (JASCO, Tokyo) with a 150-W Xe lamp as the excitation source. The slit widths are 5 nm for both the excitation and emission sides. The spectral responses were corrected in the range of 220−850 nm with a Rhodamine-B solution (5.5 g/L in ethylene glycol, for a range of 220−600 nm) and with a standard light source unit (ECS-333, JASCO, for a range of 350−850 nm) as references.

Results and Discussion

The Effects of Eu^{3+} Content on Structural Features, Morphology, and Photoluminescence Properties of the $(Y_{1-x}Eu_x)_2(OH)_5NO_3 \cdot nH_2O$ Solid Solutions. Phase composition of the hydrothermal product was found to be rather sensitive to the processing conditions. A reaction temperature of 120 °C and a final pH (the pH after reaction) of ~7.0 would yield $Y_2(OH)_5NO_3 \cdot nH_2O$ and $(Y_{1-x}Eu_x)_2(OH)_5NO_3 \cdot nH_2O$ LRH solid solutions in phase-pure forms, respectively. For x = 1.0, however, the product crystallizes as $Eu(OH)_3$ (JCPDS No. 83-2305) instead of $Eu_2(OH)_5NO_3 \cdot nH_2O$ LRH under the same conditions. Ammonium nitrate (NH_4NO_3), which provides additional NO_3^-, was found to promote the crystallization of Eu LRH, and a phase-pure product resulted at a NH_4NO_3 addition of 16 mmol (Supporting Information, Figure S1). Higher reaction temperatures of ≥160 °C (pH ~7) yielded a $(Y_{1-x}Eu_x)_4O(OH)_9NO_3$ phase (JCPDS No. 79-1352), while higher pH values of ≥8.0 (at 120 °C) would lead to either phase mixtures or pure $Ln(OH)_3$. Extending the hydrothermal time from 24 h to 168 h at 120 °C and pH ~7.0 has no obvious effects on phase purity and particle morphology of the LRH products.

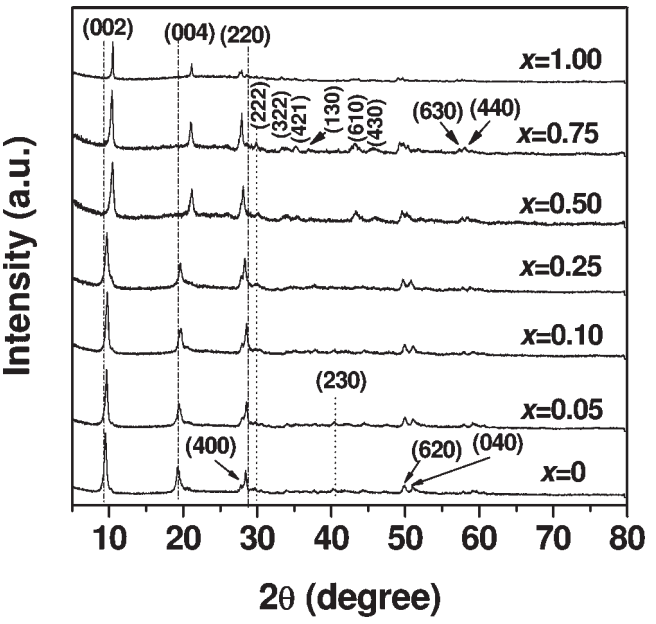

Figure 1. Powder X-ray diffraction patterns of the $(Y_{1-x}Eu_x)_2(OH)_5NO_3 \cdot nH_2O$ LRH solid solutions.

Figure 1 shows powder X-ray diffraction (XRD) patterns of the hydrothermal products with various Eu^{3+} contents. A series of strong (00l) reflections were observed to be characteristics of a layered phase, as previously reported for $Ln_2(OH)_5NO_3 \cdot nH_2O$ (RE = Sm−Tm) LRHs.[2−4] A number of weak non-(00l) reflections were also detected, indicating that the resultant LRHs are ordered.

It is interesting to find that the (00l) reflections (monitored as the (002) and (004) reflections) shift to the higher-angle side while the (hk0) reflections (monitored as the (220) reflection) to the lower angle side with increasing Eu content. The lattice constants as a function of the Eu content are plotted in Figure 2, from which it can be seen that the in-plane parameters, a and b, increase nearly monotonically with increasing Eu content, following the Vegard's law (Figures 2a, 2b). This suggests the direct crystallization of Y/Eu LRHs solid solutions. As a and b are related to the metal-to-metal distances in the host layer, the replacing of Y^{3+} with larger Eu^{3+} ions (for 6-fold coordination, $r_{Y^{3+}}$ = 0.0900 nm, $r_{Eu^{3+}}$ = 0.0947 nm)[8] would have contributed to the plane expansion. The c value (double interlayer distance) decreases at a higher Eu content, and two portions of linear relationships divided at x = 0.50, i.e. Y^{3+}/Eu^{3+} = 1:1 molar ratio, were observed (Figure 2c). Such linear relationships indicate that the interlayer distance is inversely proportional to the Eu content. The hydration

(8) Shannon, R. D. *Acta Crystallogr., Sect. A: Cryst. Phys., Diffr., Theor. Gen. Crystallogr.* **1976**, *A32*, 751.

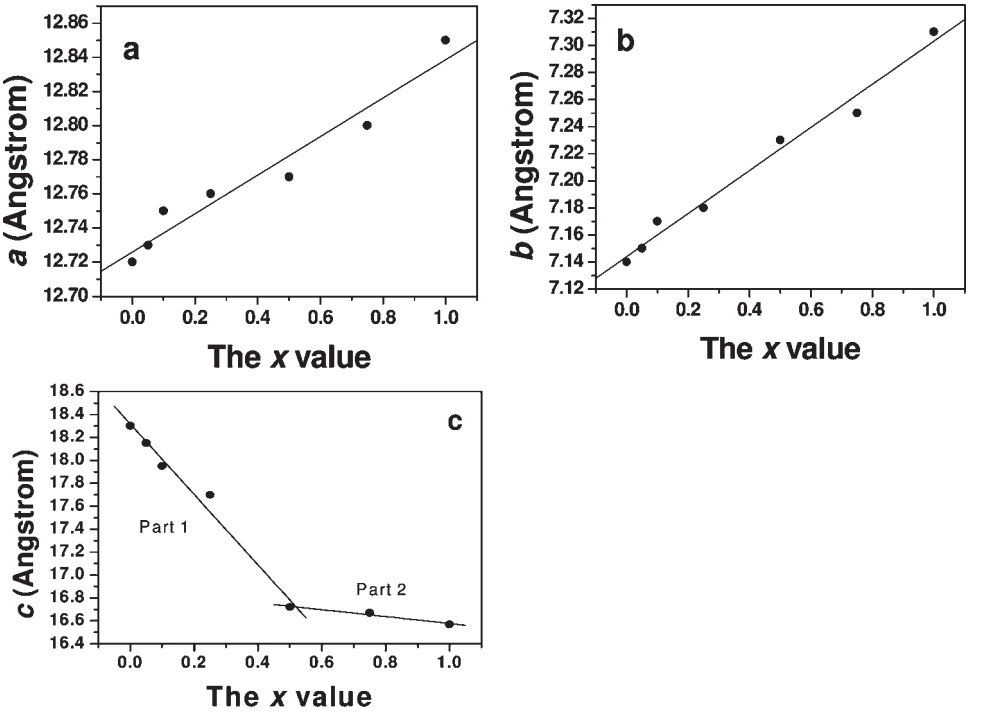

Figure 2. Correlation of the lattice parameters (a) *a*, (b) *b*, and (c) *c* with the Eu content (the *x* value in $(Y_{1-x}Eu_x)_2(OH)_5NO_3 \cdot nH_2O$).

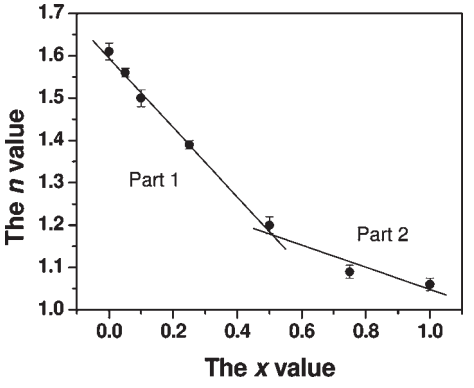

Figure 3. Number of hydration water (the *n* value in $(Y_{1-x}Eu_x)_2(OH)_5NO_3 \cdot nH_2O$), as a function of the Eu content (*x*). Each datum point is the average of three measurements, and the deviation is indicated with an error bar.

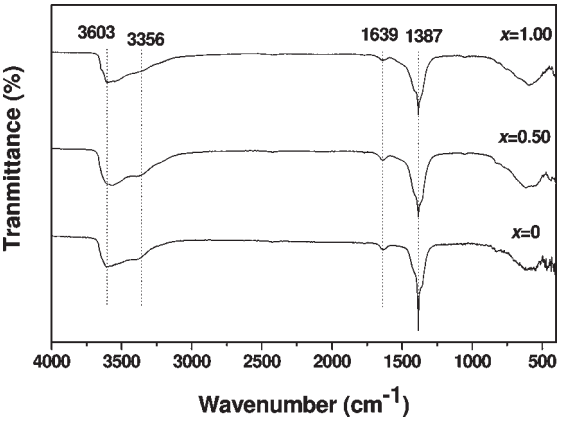

Figure 4. FT-IR spectra for three typical $(Y_{1-x}Eu_x)_2(OH)_5NO_3 \cdot nH_2O$ samples.

number *n* of $Ln_2(OH)_5NO_3 \cdot nH_2O$ was reported to decrease toward a larger Ln^{3+} (Y^{3+} and Ho^{3+} have very close ionic sizes of 0.0900 and 0.0901 nm, respectively), while a smaller number of coordinated water would lead to an appreciable contraction in the interlayer spacing. We indeed found that the LRHs crystallize as a high hydration phase of $Y_2(OH)_5NO_3 \cdot 1.61H_2O$ for Y, while a low hydration phase of $Eu_2(OH)_5NO_3 \cdot 1.06H_2O$ was observed for Eu. The hydration numbers have been determined from the TG results for the whole series of LRHs (Supporting Information, Figure S2) and are shown in Figure 3 as a function of the Eu content. Clearly, the *n* value steadily decreases with more Eu incorporation, and again two linear correlations were observed to depart at $x = 0.50$. The identical tendencies observed from Figure 2c and Figure 3 clearly indicate that the gallery height of the LRHs is closely related to the number of hydration water. The changed slopes of the two linear lines are a direct manifestation of the altered predominance of the constituent elements. When Eu becomes the major component ($x > 0.50$), the *n* value and thus the interlayer distance are dominated by the low hydration $Eu_2(OH)_5NO_3 \cdot 1.06H_2O$ phase and therefore the influences of the Y^{3+} component become weaker, yielding a less steep slope in both the cases (Part 2 in Figure 2c and Figure 3).

Figure 4 shows the FT-IR spectra of $(Y_{1-x}Eu_x)_2(OH)_5NO_3 \cdot nH_2O$ for three typical compositions. The sharp and strong absorption peak at 1387 cm^{-1} is characteristic of an uncoordinated nitrate anion and is comparable to other layered hydroxides containing interlayer nitrate groups.[2−4,9,10] The absorption peaks at ~3356 cm^{-1} and the shallow shoulder near 1639 cm^{-1} provide evidence for

(9) Nakamoto, K. *Infrared Spectra of Inorganic & Coordination Compounds*; John Wiley & Sons: New York, 1963.
(10) Gadsden, J. A. *Infrared Spectra of Minerals and Related Inorganic Compounds*; Butterworth: Newton, MA, 1975.

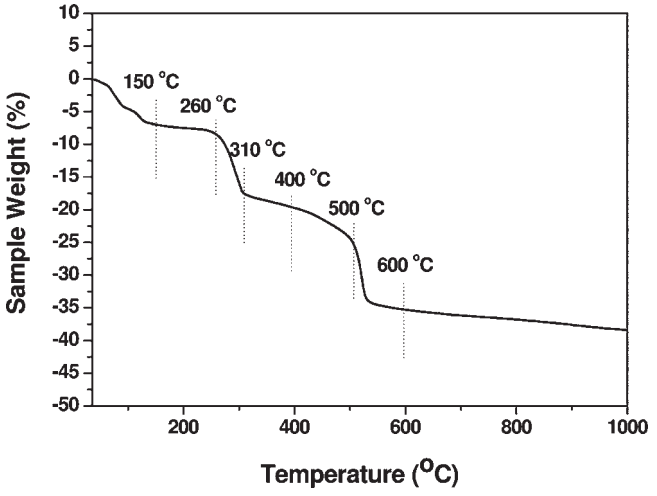

Figure 5. TG curve for $(Y_{0.95}Eu_{0.05})_2(OH)_5NO_3 \cdot 1.56H_2O$. The temperatures indicated in the figure are later used for sample annealing via ramp and holding.

water of hydration in the structure, and they are assignable to the O−H stretching vibrations (ν_1 and ν_3) and the H−O−H bending mode (ν_2), respectively.[9,10] The FT-IR spectra also suggest a decreased hydration at a higher Eu content, as seen from the weakened absorption bands at ~3356 cm^{-1} for the Eu^{3+}-rich compositions. The absorption band observed in the range 3500−3750 cm^{-1} (centered at ~3603 cm^{-1}) is indicative of hydroxyl (OH^-) groups.[9,10] The results of FT-IR spectroscopy confirm the formation of LRHs with NO_3^- intercalated between the hydroxide layers.

Thermal decomposition process of the LRHs is analyzed using the composition $(Y_{0.95}Eu_{0.05})_2(OH)_5NO_3 \cdot 1.56H_2O$ as an example, as this compound yields an oxide of the best photoluminescence upon calcination. The TG curve (Figure 5) displays three distinct stages of mass loss (total weight loss: 37.43%). Initial removal of water molecules is observed up to 260 °C with a total weight loss of 7.83%. The subsequent weight loss of 9.98% in the temperature range 260−310 °C can be attributed to dehydroxylation, which is the partial decomposition of the hydroxide layers with the loss of two water molecules, leaving behind a material of nominal composition $(Y_{0.95}Eu_{0.05})_2O_2(OH)NO_3$ (calculated weight loss: 10.02%).[2] The final step starting at 310 °C is assigned to the further decomposition of this intermediate compound to form $(Y_{0.95}Eu_{0.05})_2O_3$ solid solution.

Figure 6 shows particle morphologies of the $(Y_{1-x}Eu_x)_2(OH)_5NO_3 \cdot nH_2O$ ($x = 0-1$) solid solutions for some typical compositions, from which two effects of Eu^{3+} doping are clearly discernible. The first one is that the particle size successively decreases at a higher Eu content, particularly in the $x = 0-0.5$ range. The majority of particles in Figure 6a have lateral sizes of ~1 μm for $x = 0$, which rapidly decreases to ~400 nm in Figure 6c for $x = 0.5$. Such a tendency was previously observed in the

(11) (a) Li, J.-G.; Li, X. D.; Sun, X. D.; Ikegami, T.; Ishigaki, T. *Chem. Mater.* **2008**, *20*, 2274. (b) Krumholz, P. *Progress in the Science and Technology of the Rare Earth*; Eyring, L., Ed.; Pergamon Press: New York, 1964.

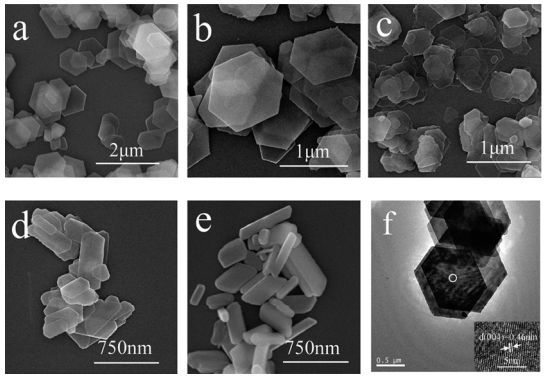

Figure 6. (a−e) FE-SEM and (f) TEM micrographs showing morphologies of the $(Y_{1-x}Eu_x)_2(OH)_5NO_3 \cdot nH_2O$ LRH solid solutions ((a) $x = 0$, (b) $x = 0.05$, (c) $x = 0.50$, (d) $x = 0.75$, and (e) $x = 1$). Pnaels (b) and (f) are from the same sample of $x = 0.05$. Inset in panel (f) is the corresponding HR-TEM lattice image.

wet-processing of $(Y_{1-x}Gd_x)_2O_3$ ($x = 0-1$) solid solutions,[11a] and it might be attributed to the higher nucleation rate of Eu^{3+} than Y^{3+} resulting from the lanthanide contraction phenomenon.[11b] Second, Eu^{3+} doping affects morphologies of the LRHs particles. Well crystallized platelets with flat surfaces, straight edges and sharp corners are generally observable for all the compositions, but the particles abruptly change from hexagons to significantly elongated shapes (see Figures 6d and 6e) when the Eu content exceeds 50 at%, that is, when Eu becomes the dominant Ln in the host layer. This phenomenon conforms to previous reports that the morphology of LRHs particles is dependent upon the ionic size of Ln^{3+}.[4c] The systematic particle morphology (size and shape) variations along with increased Eu^{3+} addition provide further evidence that LRH solid solutions are resulted directly. The sudden particle shape change when Eu exceeds 50 at. % may also correspond well to the slope changes observed in Figures 2c and 3. Figure 6f shows TEM images of the $(Y_{0.95}Eu_{0.05})_2(OH)_5NO_3 \cdot 1.56H_2O$ ($x = 0.05$) hexagons. Lattice fringes run through the whole observed area, suggesting a single crystalline nature of the plates. The resolved interplane spacing of ~0.46 nm can be well-assigned to the (004) plane of the layered crystal structure (Figure 6f, inset).

The optical properties of $Eu_8(OH)_{20}(NO_3)_4 \cdot 7H_2O$ single LRH as well as $(Gd_{1.9}Eu_{0.1})(OH)_5Cl \cdot 1.8H_2O$ and $(Gd_{1.9}Eu_{0.1})(OH)_5NO_3 \cdot nH_2O$ LRH solid solutions have been reported,[4c,5a,6] but a detailed account of the photoluminescence behaviors and especially the origins of luminescence is still lacking, particularly for a whole series of solid solutions. The PLE spectra of the LRH solid solutions, obtained by monitored the $^5D_0 \rightarrow {}^7F_2$ emission at 615 nm (Figure 7), similarly consist of a series of sharp lines ascribed to the intra-$4f^6$ transitions within the Eu^{3+} electronic configuration (Supporting Information, Figure S3). The PL spectra (Figure 7) measured through intra-$4f^6$ direct excitation at 395 nm displayed typical $^5D_0 \rightarrow {}^7F_J$ ($J = 0-4$) transitions of Eu^{3+} at 579, 589−595, 615, 653, and 698 nm, respectively. The relative intensities of the transitions to different J levels depend on the symmetry of the Eu^{3+} environment and can be described in terms of the

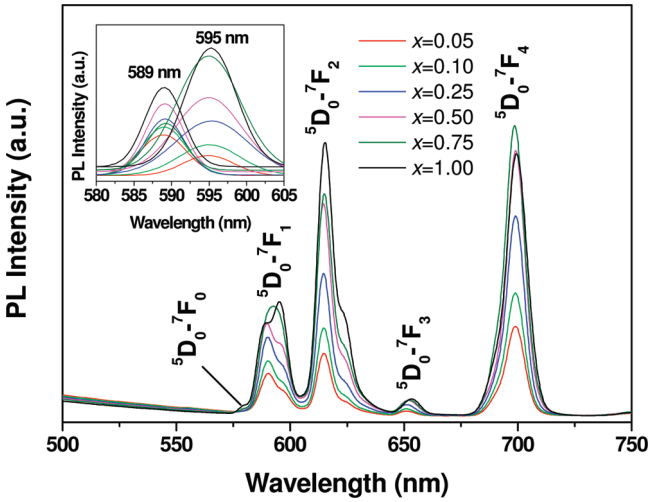

Figure 7. Photoluminescence (PL) spectra of $(Y_{1-x}Eu_x)_2(OH)_5NO_3 \cdot nH_2O$. The PL spectra are measured under intra-$4f^6$ electronic transition of Eu^{3+} at 395 nm. Inset is the two $^5D_0 \rightarrow {}^7F_1$ peaks deconvoluted by Gaussian fitting.

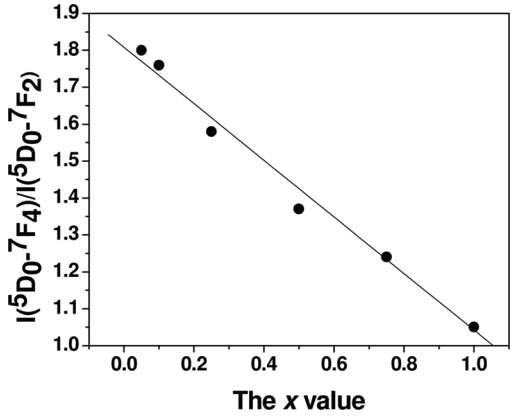

Figure 8. Correlation of the $I(^5D_0 \rightarrow {}^7F_4)/I(^5D_0 \rightarrow {}^7F_2)$ ratio with Eu content for $(Y_{1-x}Eu_x)_2(OH)_5NO_3 \cdot nH_2O$.

Judd−Ofelt theory.[12,13] Eu^{3+} luminescence from higher excited states, such as $^5D_1$, is not detected, indicating a very efficient nonradiative relaxation to the $^5D_0$ level. The $^5D_0 \rightarrow {}^7F_1$ transition retains its magnetic dipole character even in low-symmetry sites and its intensity is relatively insensitive to the coordination environment. In contrast, the $^5D_0 \rightarrow {}^7F_{2,4}$ transition is electrically dipolar in nature and the intensity of the $^5D_0 \rightarrow {}^7F_2$ emission is hypersensitive to the local chemical environment of the Eu^{3+} ion. The splitting of the $^5D_0 \rightarrow {}^7F_1$ emission band into two peaks at ~589 and 595 nm, and particularly their Eu-content-dependent intensity variations (deconvoluted in the inset of Figure 7), may indicate that there are two distinct Eu^{3+} coordination environments varying with the Y/Eu molar ratio. Sasaki et al.[4b] reported that in LRHs there are two local sites available for Ln^{3+} coordination, namely, the 4c position with 8-fold coordination $[Ln(OH)_7H_2O]$ and the 2a/2b position with 9-fold coordination $[Ln(OH)_8H_2O]$, in local symmetry groups of C_1 and C_{4v}, respectively. Because the number of Ln^{3+} cation species at C_{4v} is twice that at C_1 site[4a] and Eu^{3+} is expected to substitute for Y^{3+} in a statistic way, the stronger 589 nm emission (than the 595 nm emission observed for the $x = 0.05$ composition) may thus imply that the former largely originates from the Eu^{3+} activators occupying C_{4v}, while the latter from the Eu^{3+} residing at C_1. These assignments are also supported by the systematic intensity variations of the two $^5D_0 \rightarrow {}^7F_1$ emissions in the composition range $0.05 \leq x \leq 1.0$. Although the intensity of the $^5D_0 \rightarrow {}^7F_1$ transition steadily increases at a higher Eu content, the 595 nm emission gradually gains strength over the 589 nm one and, finally, the relative intensity of the two peaks is reversed at $x = 1.0$, suggesting coordination environment changes of Ln with more Eu incorporation. In LRHs, as previously discussed, the water molecules are directly coordinated to the Ln atoms forming coordination polyhedra instead of being intercalated in the interlayer as free water.[4] The water molecules have priority to occupy the $[Ln(OH)_7H_2O]$ dodecahedron, instead of the $[Ln(OH)_8H_2O]$ monocapped square antiprism.[1,4] The loss of hydration water at a higher Eu content would thus shift the Ln^{3+} cations from 9-fold coordination to 8-fold coordination, yielding more Eu^{3+} activators having C_1 symmetry. This would account for the observed relative intensity changes of the two $^5D_0 \rightarrow {}^7F_1$ emission peaks, and further confirm that the C_{4v}- and C_1-site Eu^{3+} significantly contribute to the 589 and 595 nm emissions, respectively.

We now must account for the origins of the two main emission bands of $^5D_0 \rightarrow {}^7F_{2,4}$. The group-theory selection rules of C_{4v} symmetry do not allow the occurrence of $^5D_0 \rightarrow {}^7F_{2,4}$ electric-dipole transitions with intensities greater than the magnetic-dipole $^5D_0 \rightarrow {}^7F_1$ transition.[14−16] The much-stronger $^5D_0 \rightarrow {}^7F_{2,4}$ emissions observed in this work thus imply that the C_1-site Eu^{3+} have substantially contributed to these two bands, although the exact extent is unknown. The lower emission intensity of $^5D_0 \rightarrow {}^7F_2$ than that of the $^5D_0 \rightarrow {}^7F_4$ transition observed for all the compositions except for $x = 1.0$ suggest that there are indeed simultaneous contributions from the C_{4v}-site Eu^{3+}, particularly to the $^5D_0 \rightarrow {}^7F_4$ emission at ~700 nm.[14−16] The intensity of the $^5D_0 \rightarrow {}^7F_2$ transition at ~615 nm improves monotonically with increasing Eu content, while that of the $^5D_0 \rightarrow {}^7F_4$ transition first increases up to 75 at. % Eu and then drops. We analyzed the integrated intensities of these two peaks, and the ratio $I(^5D_0 \rightarrow {}^7F_4)/I(^5D_0 \rightarrow {}^7F_2)$ are displayed in Figure 8, as a function of the Eu content, where an almost-linear decrease of the ratio from ~1.80 at $x = 0.05$ to ~1.05 at $x = 1.0$ is clearly seen. As discussed earlier, enhanced Eu incorporation in the LRHs solid solution yields fewer hydration water molecules and thus leads to a partial shift of the Ln^{3+} from C_{4v} to C_1 sites. The decreasing $I(^5D_0 \rightarrow {}^7F_4)/I(^5D_0 \rightarrow {}^7F_2)$ intensity ratio is thus ascribed to the migration of Eu^{3+} activators from the C_{4v} to C_1 coordination environments.

(12) Judd, B. R. *Phys. Rev.* **1962**, *127*, 750.
(13) Ofelt, G. S. *J. Chem. Phys.* **1962**, *37*, 511.
(14) Blasse, G.; Dirksen, G. J.; Zonnevijlle, F. *J. Inorg. Nucl. Chem.* **1981**, *43*, 2847.
(15) Sugeta, M.; Yamase, T. *Bull. Chem. Soc. Jpn.* **1993**, *66*, 444.
(16) Sa Ferreira, R. A.; Nobre, S. S.; Granadeiro, C. M.; Nogueira, H. I. S.; Carlos, L. D.; Malta, O. L. *J. Lumin.* **2006**, *121*, 561.

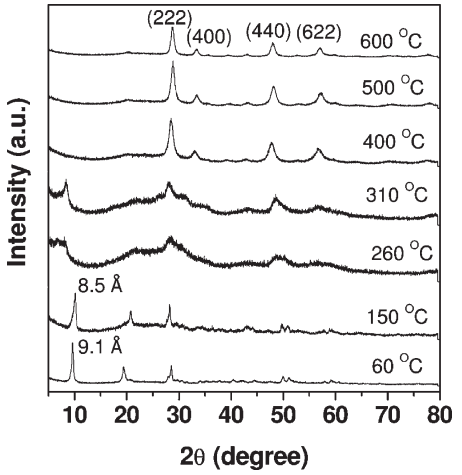

Figure 9. XRD patterns of the products calcined from $(Y_{0.95}Eu_{0.05})_2(OH)_5NO_3 \cdot 1.56H_2O$ at the various temperatures indicated in the figure.

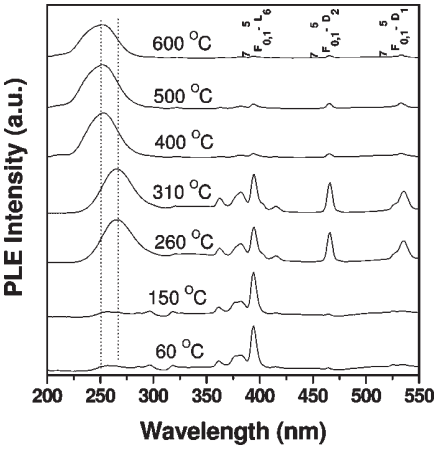

Figure 10. Photoluminescence excitation spectra of $(Y_{0.95}Eu_{0.05})_2(OH)_5NO_3 \cdot 1.56H_2O$ calcined at the various temperatures indicated in the figure. The PLE spectra are obtained by monitoring the 615 nm emission for the samples at 60−150 °C and the 613 nm emission for the others.

The above observations also indicate that the $^5D_0 \rightarrow {}^7F_4$ transition is more significantly associated with the C_{4v}-site Eu^{3+} while the $^5D_0 \rightarrow {}^7F_2$ emission more significantly with the C_1-site Eu^{3+} ions.

Enhanced emission was generally observed at a higher Eu content via the direct excitation of Eu^{3+} at 395 nm (Figure 7). This phenomenon has been attributed to the increased number of emission centers and absorption cross section of Eu^{3+}, which allows radiation to be the more prominent relaxation process than the nonradiative relaxation via concentration quenching.[5d]

Structural Evolution of $(Y_{1-x}Eu_x)_2(OH)_5NO_3 \cdot nH_2O$ upon Calcination and the Related PL/PLE Phenomena. Phase evolution of the LRH solid solutions upon annealing was studied in the range of 60−600 °C with the sample $(Y_{0.95}Eu_{0.05})_2(OH)_5NO_3 \cdot 1.56H_2O$ as an example (Figure 9). These typical calcination temperatures were determined according to the TG analysis and have been marked in Figure 5. The layered structure maintained at 150 °C and, at this temperature, a low hydration phase having an approximate composition of $(Y_{0.95}Eu_{0.05})_2(OH)_5NO_3 \cdot 1.26H_2O$ resulted. The 150 °C sample shows PL/PLE spectra (see Figures 10 and 11) typical of the LRH solid solutions (Figure 7). Because of dehydration, however, the interlayer spacing is reduced from ~0.91 nm to ~0.85 nm and the sample shows $^5D_0 \rightarrow {}^7F_{1,2,4}$ transitions of varied relative intensities. It was found that, for integrated intensities, the $I(^5D_0 \rightarrow {}^7F_4)/I(^5D_0 \rightarrow {}^7F_2)$ ratio decreased from ~1.8 to 1.36 while the I_{595}/I_{589} ratio increased from ~0.45 to 0.85, along with a loss of ~0.3 mol per chemical formula of H_2O from 60 to 150 °C. These findings further support our assignments of the PL bands to different Eu^{3+} local environments and add weight to our arguments that less hydration at a higher Eu content would shift the coordination symmetry from C_{4v} to C_1. Enhanced overall luminescence was observed from 60 °C to 150 °C, because of the loss of hydration water, which is know to effectively quench luminescence. This also suggests that the decreased hydration at a higher Eu content may have also contributed to the nonquenching phenomena observed in Figure 7.

The layered structure collapses at a higher annealing temperature of 260 °C as a result of the partial dehydroxylation of the hydroxide host layers (Figure 9), yielding a low-crystallinity mass having a calculated composition of $(Y_{0.95}Eu_{0.05})_2O_2(OH)NO_3$.[2] The PLE spectrum of the 260 °C sample indeed shows, besides the still relatively strong intra-$4f^6$ transitions, the occurrence of $O^{2-}-Eu^{3+}$ charge transfer band (CTB) arising from dehydroxylation, which induces one O^{2-} substituting for two OH^- coordinated to Eu^{3+}. Increasing to 310 °C yields no significant structural changes (Figure 9). Both the PLE/PL spectra of the 260 and 310 °C samples exhibit features midway between those of the LRHs precursors and the $(Y_{0.95}Eu_{0.05})_2O_3$ solid solutions (see Figures 10 and 11).

Further decomposition of the $(Y_{0.95}Eu_{0.05})_2O_2(OH)NO_3$ intermediate happened above 310 °C, and almost all the diffraction peaks corresponding to the cubic structured Y_2O_3 (JCPDS No. 89-5591) have appeared at 400 °C (Figure 9). The slight shift of the diffraction peaks toward the lower-angle side is possibly due to the incomplete decomposition, particularly of NO_3^-, as suggested by TG (Figure 5). In the range of 400−600 °C, the samples demonstrate PLE/PL spectra typical of Eu^{3+}-activated Y_2O_3, characterized by a strong CTB, while weak intra-$4f^6$ excitations (Figure 10) and dominant red emissions at ~613 nm arising from the $^5D_0 \rightarrow {}^7F_2$ forced electric dipole transitions of Eu^{3+} in the Y_2O_3 host (see Figures 11c and 11d). As marked in the figure, other emission bands were observed, corresponding to the following: the $^5D_0 \rightarrow {}^7F_0$ transition at 582 nm; the magnetic dipole $^5D_0 \rightarrow {}^7F_1$ transition at ~589, 595, and 601 nm (three Stark splits); the $^5D_0 \rightarrow {}^7F_3$ transition at 652 nm; and the $^5D_0 \rightarrow {}^7F_4$ transition at ~710 nm. The decreased relative intensity of the $^5D_0 \rightarrow {}^7F_4$ transition from 400 °C to 600 °C is due to the further removal of hydroxyl and nitrate residues, which distorts the crystal field. Under identical measuring conditions, it was found that raising the annealing temperature from 60 °C to 600 °C produced an ~1750-fold increase in the intensity of the 613-nm emission.

Structures, Morphology, and Photoluminescence Properties of the $(Y_{1-x}Eu_x)_2O_3$ Solid Solutions (x = 0−1). Figure 12 demonstrates XRD patterns of the oxides

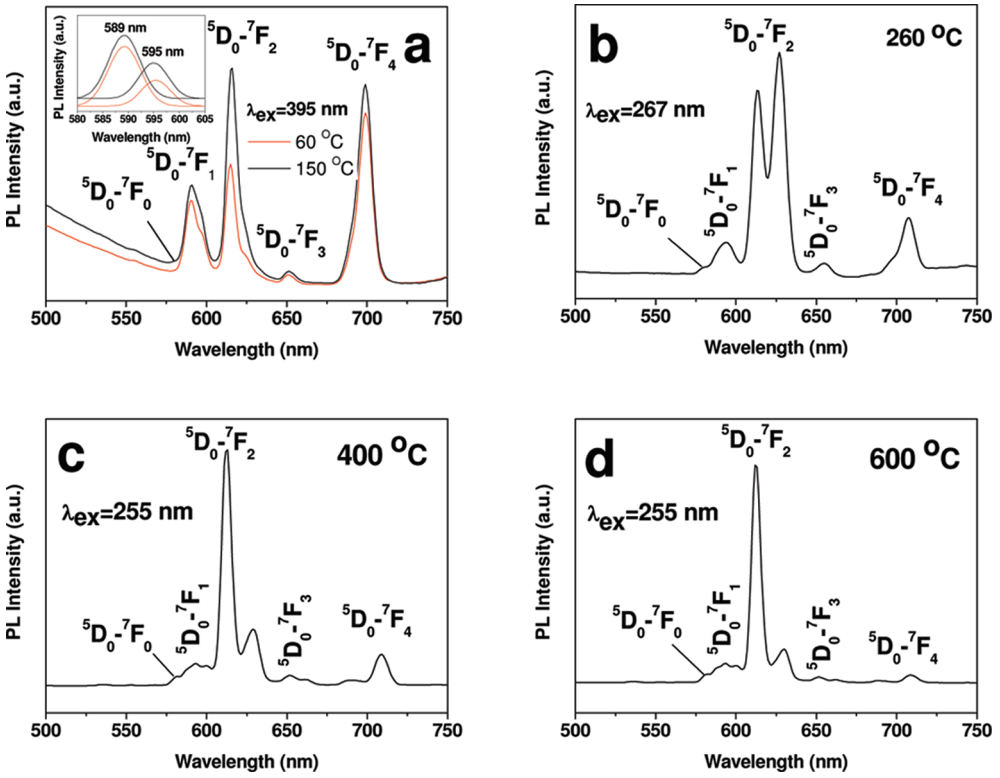

Figure 11. Photoluminescence spectra of $(Y_{0.95}Eu_{0.05})_2(OH)_5NO_3 \cdot 1.56H_2O$ calcined at the various temperatures indicated in panels (a)−(d). Inset in panel (a) shows the two $^5D_0 \rightarrow {}^7F_1$ peaks deconvoluted by Gaussian fitting.

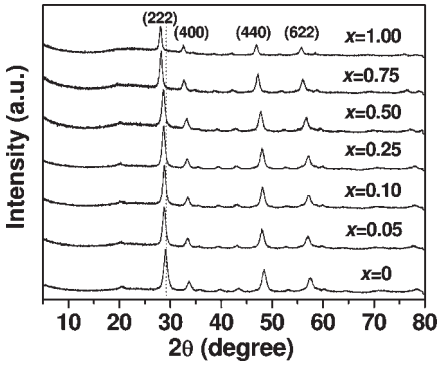

Figure 12. XRD patterns of $(Y_{1-x}Eu_x)_2O_3$ calcined from $(Y_{1-x}Eu_x)_2(OH)_5NO_3 \cdot nH_2O$ at 600 °C for 4 h.

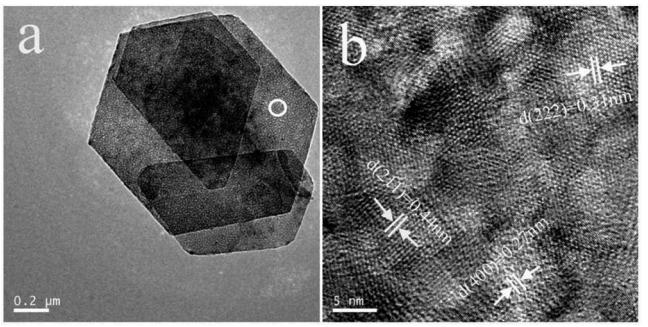

Figure 13. (a) TEM and (b) HR-TEM micrographs for the $(Y_{0.95}Eu_{0.05})_2O_3$ sample calcined at 600 °C for 4 h.

obtained by calcination at 600 °C for 4 h. No other phase was identified along with the cubic structured $(Y_{1-x}Eu_x)_2O_3$ ($x = 0-1$) (Y_2O_3, JCPDS No. 89-5591). The XRD peaks steadily shift toward the low-angle side with increasing Eu addition, indicating a gradually expanded unit cell of the crystal structure, which is due to the incorporation of larger Eu^{3+} ions.[8] The lattice constant of the $(Y_{1-x}Eu_x)_2O_3$ ($x = 0-1$) oxide follows the Vegard's law and linearly increases along with the value of x increasing from 0 to 1. This indicates the already formation of solid solutions at this rather low annealing temperature, because of the atomic level homogeneous mixing of Y^{3+} and Eu^{3+}. The resultant oxides well-retained the original morphologies of their respectively precursors (Supporting Information, Figure S4), showing shapes very beneficial to the construction of luminescent films via further processing. HR-TEM analysis conformed that the oxides are of polycrystalline, as shown in Figure 13 with the composition $(Y_{0.95}Eu_{0.05})_2O_3$ as an example. The platelets are made up of nanocrystals with sizes of up to ~10 nm, and lattice spacing analysis confirmed the exposure of (222), (211), and (400) facets.

Figure 14 shows PLE/PL spectra of the $(Y_{1-x}Eu_x)_2O_3$ solid solutions. As mentioned earlier, the strong excitation bands with maxima at 251−272 nm (Figure 14a) are the transitions by charge transfer (CT), that is, the electronic transition from the 2p orbital of O^{2-} to the 4f orbital of Eu^{3+} activators. The four groups of excitation peaks at longer wavelengths are the intra-4f electronic transitions of Eu^{3+}, as found in the PLE spectra of the LRHs solid solutions (Supporting Information, Figure S3). In the charge transfer excitation, the O^{2-} 2p electrons are excited into the 4f levels of Eu^{3+}, and the position of the CT band is determined by the energy difference between the O^{2-} 2p valence band and the 4f levels of

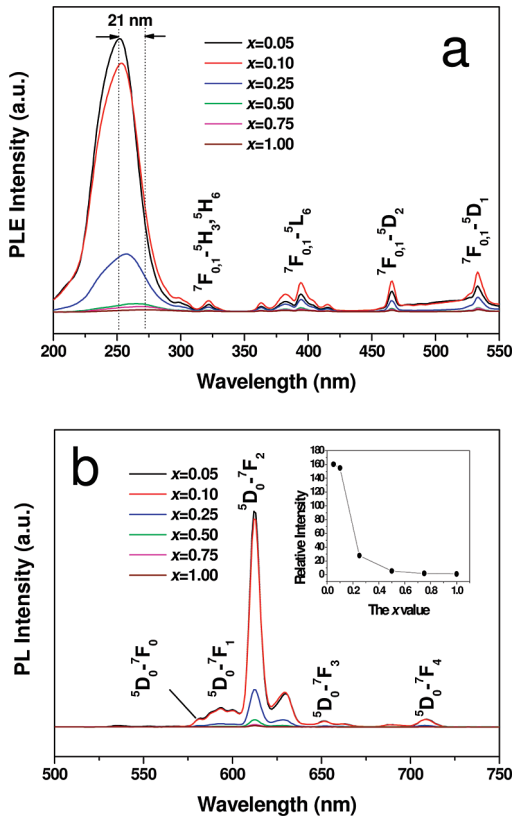

Figure 14. (a) Photoluminescence excitation (PLE) and (b) photoluminescence (PL) spectra of the $(Y_{1-x}Eu_x)_2O_3$ solid solutions calcined at 600 °C for 4 h. The PLE spectra are obtained by monitoring the 613 nm emission, while the PL spectra are measured under 255 nm excitation. Inset in panel (b) shows the relative intensities obtained by normalizing the observed 613-nm PL intensities, relative to that of the Eu_2O_3 ($x = 1$) sample.

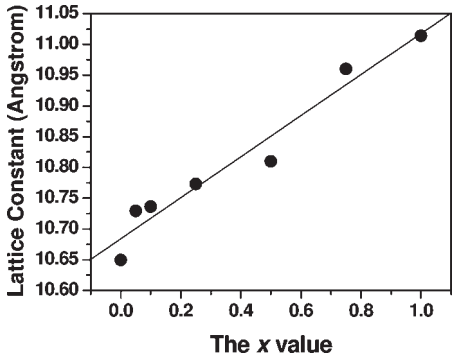

Figure 15. Lattice constant of $(Y_{1-x}Eu_x)_2O_3$, as a function of the Eu content (x).

Eu^{3+}. The 4f orbital is not involved in the bonding between rare-earth ions and the ligands. The interaction between the Eu^{3+} 5d and O^{2-} 2p orbitals, however, leads to bonding (2p) and antibonding (5d) molecular orbitals. Therefore, one could expect that the shorter the Eu−O bond, the larger the energy difference between the Eu^{3+} 4f and O^{2-} 2p electrons.[18] The successive shifting of the CT band center from ~251 nm to ~272 nm with increasing Eu content (see Figure 14a) indicates a decreased energy difference between the Eu^{3+} 4f and O^{2-} 2p electrons, and this is due to the increased Eu−O bond length, as expected from the lattice expansion (Figure 15). Upon UV excitation at 255 nm, the oxide solid solutions exhibit sharp lines ranging from 500 nm to 750 nm, which are associated with the transitions from the excited $^5D_0$ to the ^7F_J ($J = 0, 1, 2, 3, 4$) emission states of Eu^{3+}.[17] The red emission at 613 nm is arising from the hypersensitive $^5D_0 \rightarrow {}^7F_2$ forced electric dipole transition as commonly observed. The best luminescence was observed for $x = 0.05$ and the performance deteriorates drastically when the Eu content exceeds 10 at. % (see Figure 14 and the inset). The observed luminescence intensities conform well to the CT band intensities for all the samples. As previously discussed, the Eu−O bond length becomes longer at a higher Eu^{3+} content, which decreases the probability of O^{2-}−Eu^{3+} CT transition. Furthermore, the distance among the adjacent Eu^{3+} ions becomes shorter with more Eu^{3+} incorporation and thus the probability of energy transfer among the Eu^{3+} activators themselves is enhanced,[17,19,20] contributing to the significant luminescence quenching at $x > 0.1$.

The cubic Y_2O_3 lattice is known to have two different crystallographic positions for Eu^{3+} substitution: the 24d (C_2) site without inversion symmetry and the 8b (S_6) site with inversion symmetry. The ratio of C_2 to S_6 is 3:1 and the Eu^{3+} activators are expected to take these two sites in a statistical way, upon replacing Y^{3+}. The Judd−Ofelt parity law predicts that the magnetic dipole transition is permitted while the electric dipole transition forbidden, and the latter is allowed only on the condition that the Eu^{3+} ions occupy a site without an inversion center. The higher occupancy of Eu^{3+} at the noncentrosymmetric C_2 sites (75%) thus yields a PL spectrum dominated by the $^5D_0 \rightarrow {}^7F_2$ electric dipole transition at ~613 nm, and the S_6-site Eu^{3+} can only contribute to the $^5D_0 \rightarrow {}^7F_1$ magnetic dipole transition. Because the $^5D_0 \rightarrow {}^7F_2$ transition is hypersensitive to the local Eu^{3+} environment while $^5D_0 \rightarrow {}^7F_1$ not, the intensity ratio $I(^5D_0 \rightarrow {}^7F_2)/I(^5D_0 \rightarrow {}^7F_1)$—which is called the asymmetry factor—has been effectively used to probe the local coordination environment of Eu^{3+}. We analyzed the asymmetry factor for the whole series of oxide solid solutions, and the results are plotted in Figure 16, as a function of the Eu content. The factor clearly remains almost constant at ~11.4 up to $x = 0.5$ and then rapidly increases to ~23 at $x = 1.0$. Decreased size of the phosphor particles would generate more Eu^{3+} on the particle surfaces, because of the surface/volume effects, and the loss of centrosymmetry of these activators would allow a stronger $^5D_0 \rightarrow {}^7F_2$, but a weaker $^5D_0 \rightarrow {}^7F_1$ transition and, thus, a higher asymmetry factor. This, however, cannot be excluded and may not be the major cause for what is observed from Figure 16, since no

(17) Li, J.-G.; Li, X. D.; Sun, X. D.; Ishigaki, T. *J. Phys. Chem. C* **2008**, *112*, 11707.
(18) (a) Lin, J. H.; You, L. P.; Lu, G. X.; Yang, L. Q.; Su, M. Z. *J. Mater. Chem.* **1998**, *8*, 1051. (b) Hoefdraad, H. E. *J. Solid-State Chem.* **1975**, *15*, 175.
(19) Blasse, G. *Philips Res. Rep.* **1969**, *24*, 131.
(20) Yuan, J.-L.; Zeng, X.-Y.; Zhao, J.-T.; Zhang, Z.-J.; Chen, H.-H.; Zhang, G.-B. *J. Solid-State Chem.* **2007**, *180*, 3310.

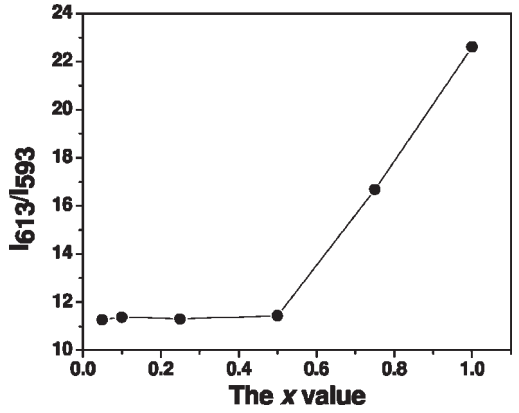

Figure 16. $I(^5D_0 \rightarrow {}^7F_2)/I(^5D_0 \rightarrow {}^7F_1)$ ratio (the luminescence asymmetry factor) for the $(Y_{1-x}Eu_x)_2O_3$ phosphors calcined at 600 °C for 4 h, as a function of the Eu content.

appreciable change in the factor resulted as the particle size decreased from ~1.0 μm at $x = 0.05$ to ~400 nm at $x = 0.5$ (Supporting Information, Figure S4). In solid-state chemistry, it is known that the coordination environment of a cation is significantly affected by the cation−anion distance, and the chemical bonding shifts to lower energies with increasing bond length.[18b] Sheng et al.[21] reported the appearance of a new symmetry site of C_1, distorted from S_6, for Eu^{3+} in a nanocrystalline Eu_2O_3 bcc lattice. In contrary to the widely accepted 6-fold coordination in bulk bcc Eu_2O_3, the C_1 symmetry possesses 8-fold coordination and has no inversion center. Qi et al.[25] also found that the Eu^{3+} activator in Y_2O_3:Eu^{3+} may have 8-fold coordination if the Eu−O bond is elongated at the high surface area (small crystallite size) of the sample. It was also shown that the 8-fold coordination appears more readily in nanocrystalline Eu_2O_3 than in Y_2O_3, because of the longer bond length of the former.[22] From these, the appearance of noncentrosymmetric C_1-site Eu^{3+} might account for the abrupt increase in the asymmetry factor at $x > 0.5$, since it would enhance the $^5D_0 \rightarrow {}^7F_2$ electric dipole transition while lowering the $^5D_0 \rightarrow {}^7F_1$ magnetic dipole emission at the same time. This is made possible by the fine crystallites of the sample (up to ~10 nm, Figure 13) and when Eu becomes the major component ($x > 0.50$).

Conclusions

In the present work, a whole series of $(Y_{1-x}Eu_x)_2(OH)_5NO_3 \cdot nH_2O$ ($x = 0-1$) LRH solid solutions have been successfully synthesized via hydrothermal reactions, which were then converted to oxide phosphors via calcination. Detailed characterizations of the products by combined techniques of XRD, TG, FT-IR, FE-SEM, HR-TEM, and PLE/PL have yielded the following main conclusions:

(1) Well-crystallized LRHs hexagons can be obtained under the optimal processing conditions of 120 °C and pH ~7.0. The two extreme compositions crystallize as a high hydration phase of $Y_2(OH)_5NO_3 \cdot 1.61H_2O$ for Y but as a low hydration phase of $Eu_2(OH)_5NO_3 \cdot 1.06H_2O$ for Eu. The intermediate composition possesses a hydration number (n) that is inversely proportional to the Eu content, in two trends divided at $x = 0.5$. Size of the LRHs particles decreases with increasing Eu content, and the particle shape changes from hexagons to elongated ones at $x > 0.5$. The in-plane lattice parameters, a and b, linearly increase with increasing Eu incorporation, following the Vegard's law. The interlayer distance ($c/2$) shrinks at a higher Eu content due to the lowered hydration, following the tendency observed for the Eu-dependent variations of hydration number n. Decreased hydration shifts the coordination environment of Eu^{3+} from C_{4v} to C_1 symmetries, thus leading to the systematically varied photoluminescence behaviors of the LRH solid solutions. The C_1-site Eu^{3+} ions are found to be significantly associated with the 595 nm $^5D_0 \rightarrow {}^7F_1$ transition and the $^5D_0 \rightarrow {}^7F_2$ transition at 615 nm, while the C_{4v}-stite Eu^{3+} ions are associated with the 589 nm $^5D_0 \rightarrow {}^7F_1$ transition and the $^5D_0 \rightarrow {}^7F_4$ transition at 698 nm.

(2) The LRHs convert to cubic solid solutions of $(Y_{1-x}Eu_x)_2O_3$ at temperatures of ≥400 °C via a $(Y_{1-x}Eu_x)_2O_2(OH)NO_3$ intermediate while retaining the original particle morphologies. The oxide with $x = 0.05$ exhibits the best luminescence for the 613-nm red emission under UV excitation at 255 nm, and significant luminescence quenching was observed at $x > 0.10$.

(3) The lattice constant of $(Y_{1-x}Eu_x)_2O_3$ increases almost linearly with the Eu^{3+} content, inducing longer Eu−O bond length, which contributes to the red shift of the charge-transfer excitation band of luminescence. The asymmetry factor of luminescence, $I(^5D_0 \rightarrow {}^7F_2)/I(^5D_0 \rightarrow {}^7F_1)$, keeps nearly constant at ~11.4 up to $x = 0.5$, followed by a sharp increase to ~23 at $x = 1.0$, which has been ascribed to the splitting of C_1 symmetry from distorted S_6 sites in $(Y_{1-x}Eu_x)_2O_3$ at $x > 0.5$.

Acknowledgment. This work has been supported by the National Natural Science Foundation of China (Grants 50972025 and 50990303), the Educational Department of Liaoning Province, the Special Fund for Basic Research in Central Universities (Grant N090502001), the Program for Changjiang Scholars and Innovative Research Teams in University (PCSIRT, IRT0713), and Grant-in-Aid for Scientific Research (KAKENHI, No. 22550135).

Supporting Information Available: XRD patterns of the Eu-based hydrothermal products ($x = 1.0$) with various NH_4NO_3 additions, TG curves for $(Y_{1-x}Eu_x)_2(OH)_5NO_3 \cdot nH_2O$ and the determination of the number (n) of hydration water, PLE spectra of the $(Y_{1-x}Eu_x)_2(OH)_5NO_3 \cdot nH_2O$ LRH solid solutions, and SEM images of the $(Y_{1-x}Eu_x)_2O_3$ solid solutions calcined from $(Y_{1-x}Eu_x)_2(OH)_5NO_3 \cdot nH_2O$ at 600 °C for 4 h. These materials are available free of charge via the Internet at http://pubs.acs.org.

(21) Sheng, K. C.; Kornowski, G. M. *J. Phys. Chem.* **1988**, *92*, 50.
(22) Qi, Z. M.; Shi, C. S.; Zhang, W. W.; Zhang, W. P.; Hu, T. D. *Appl. Phys. Lett.* **2002**, *81*, 2857.